

Article

Digital-Twin-Based Coordinated Optimal Control for Steel Continuous Casting Process

Jian Yang ^{1,2,*} , Zhenping Ji ³, Wenhong Liu ^{1,2}  and Zhi Xie ^{1,2}

- ¹ College of Information Technology and Engineering, Northeastern University, Shenyang 110819, China
² Engineering Research Center of Digital Instrumentation for Process Industries (Ministry of Education), Shenyang 110819, China
³ College of Information Technology and Engineering, Shenyang Ligong University, Shenyang 110159, China
* Correspondence: neuyangjian@163.com

Abstract: A digital-twin-model-based optimal control system is presented for the steel continuous casting process. The system is designed for the coordinated optimization and dynamic control of secondary cooling and final electromagnetic stirring (FEMS), and involves three related parts. Firstly, a three dimensional real-time heat transfer model is established as the digital twin of the heat transfer process of continuous casting; for high accuracy, it is calibrated offline and calibrated online using measurements of the surface temperatures and shell thicknesses (only offline). Secondly, according to metallurgical rules, cooling and stirring are optimized coordinatively, based on the established digital-twin model and chaos particle swarm optimization algorithm. Thirdly, cooling and stirring are further dynamically controlled for quality stability. Finally, the system is applied in a bloom caster with model errors $\leq \pm 10$ °C and control errors $\leq \pm 4$ °C, which reduces the macro-segregation over grade 1.5 from 11% to 3.3%.

Keywords: digital twin; optimal control; continuous casting; cooling; stirring; heat transfer



Citation: Yang, J.; Ji, Z.; Liu, W.; Xie, Z. Digital-Twin-Based Coordinated Optimal Control for Steel Continuous Casting Process. *Metals* **2023**, *13*, 816. <https://doi.org/10.3390/met13040816>

Academic Editor: Noé Cheung

Received: 20 February 2023

Revised: 15 April 2023

Accepted: 19 April 2023

Published: 21 April 2023



Copyright: © 2023 by the authors. Licensee MDPI, Basel, Switzerland. This article is an open access article distributed under the terms and conditions of the Creative Commons Attribution (CC BY) license (<https://creativecommons.org/licenses/by/4.0/>).

1. Introduction

Nowadays, continuous casting is the predominant way to produce solidified steel ingots from molten steel. During the continuous casting process, both secondary cooling and final electromagnetic stirring (FEMS) play vital roles in product quality, as they greatly influence the heat transfer and flow process during solidification.

The continuous casting process is schematically shown in Figure 1. In the process, molten steel is poured into the water-cooled copper mold from a tundish, where the initial solidified shell forms, which involves solidifying the molten steel inside. After passing through the mold, the shell enclosing the molten steel moves down into the secondary cooling zones (SCZ), where further cooling takes place by water sprays from nozzles, and the shell grows increasingly. On exit from the SCZ, the strand cools off by radiation in the air and finishes the solidification gradually. Finally, the strand is cut into segments of fixed length, and transported for rolling. During the process, secondary cooling is vital for temperature distribution and greatly influences the strand quality. In addition, to further improve the strand quality, electromagnetic stirring is commonly used, including mold electromagnetic stirring (MEMS), secondary cooling electromagnetic stirring (SEMS) and final electromagnetic stirring (FEMS). Among these, FEMS especially is supposed to be the key to improving the central quality of products, such as central segregation, porosity and shrinkage, etc. [1].

For optimal control of secondary cooling and final electromagnetic stirring, the heat transfer model is fundamental to calculate the solidification states inside and outside. In recent years, much research has been carried out well into the heat transfer model [2–7]. Among these studies, most of the developed models are two-dimensional [8] or three dimensional but offline [9], and the steady models are applied to optimize the

process parameters [10,11], while real-time transient ones are used for online dynamic control [12,13]. However, for more precise control, the model is supposed to be three dimensional and real-time. In particular, during the initial casting stage and final casting stage, the heat transfer along the casting direction is too obviously near the bottom surface or top surface to be ignored.

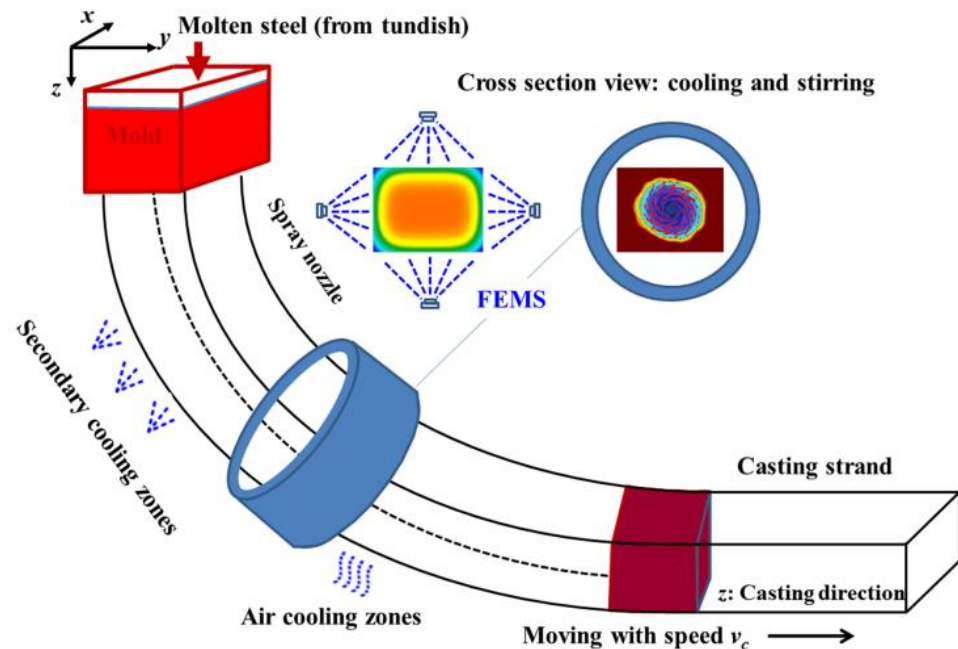


Figure 1. Continuous casting process.

Conventionally, secondary cooling and FEMS are treated as two independent technologies without considering their interaction, and their parameters are generally optimized separately [14–16]. The optimization depends on conventional optimization algorithms and plant trials. Beyond optimization, dynamic control of secondary cooling and electromagnetic stirring further benefits the quality of the stability. Dynamic control can reduce the fluctuation of solidification states during transient situations [8,12,17]. In practice, due to the conflicts of multiple technologies and fluctuations under static control, the actual quality may not be the best. In 2020, Ji et al. [18] presented a coordinated optimal control strategy based on a multiobjective particle swarm optimization (MOPSO) algorithm (our previous work), which mainly focuses on the optimization algorithm and is not precise enough in model form and not practical enough regarding metallurgical knowledge.

Therefore, in this paper, aiming at improving and stabilizing the product quality of steels and considering the conflicting multi-objectives, a coordinated optimization and dynamic control system was developed, and it was based on a high-accuracy three dimensional real-time heat transfer model for all stages of the continuous casting process. Firstly, a three dimensional real-time heat transfer model was established as the digital twin; for high accuracy, it was calibrated offline and online by measurements of surface temperatures and shell thicknesses. Secondly, according to metallurgical rules, cooling and stirring were coordinated and optimized based on a high-accuracy model and the chaos particle swarm optimization algorithm. Thirdly, cooling and stirring were further dynamically controlled for quality stability. Finally, the optimal control system was applied to a bloom caster, which greatly improved the product quality.

2. Overview of Optimal Control Framework

The digital-twin-model-based framework for optimal control of secondary cooling and FEMS is shown in Figure 2. The framework includes three parts: the fundamental high-accuracy model, the coordinated optimization, and dynamic control of cooling and stirring.

Above all, the high-accuracy heat transfer model serves as the basis of both optimization and control parts, providing calculated solidification states such as surface temperatures and liquid core radius. In the model part, for high accuracy, the model is calibrated offline and online by surface temperature measurements and shell thickness measurements. In the optimization part, a multi-objective optimization problem is established based on metallurgical rules, and then it is solved by the particle swarm optimization algorithm. In the dynamic control part, secondary-cooling water flows and FEMS' stirring current are dynamically controlled, based on the calculations of the online model, to avoid fluctuations in surface temperature and flow velocity in the solidification frontier, and this benefits the quality of the stability. Moreover, optimization provides the setpoints and coefficients for dynamic control.

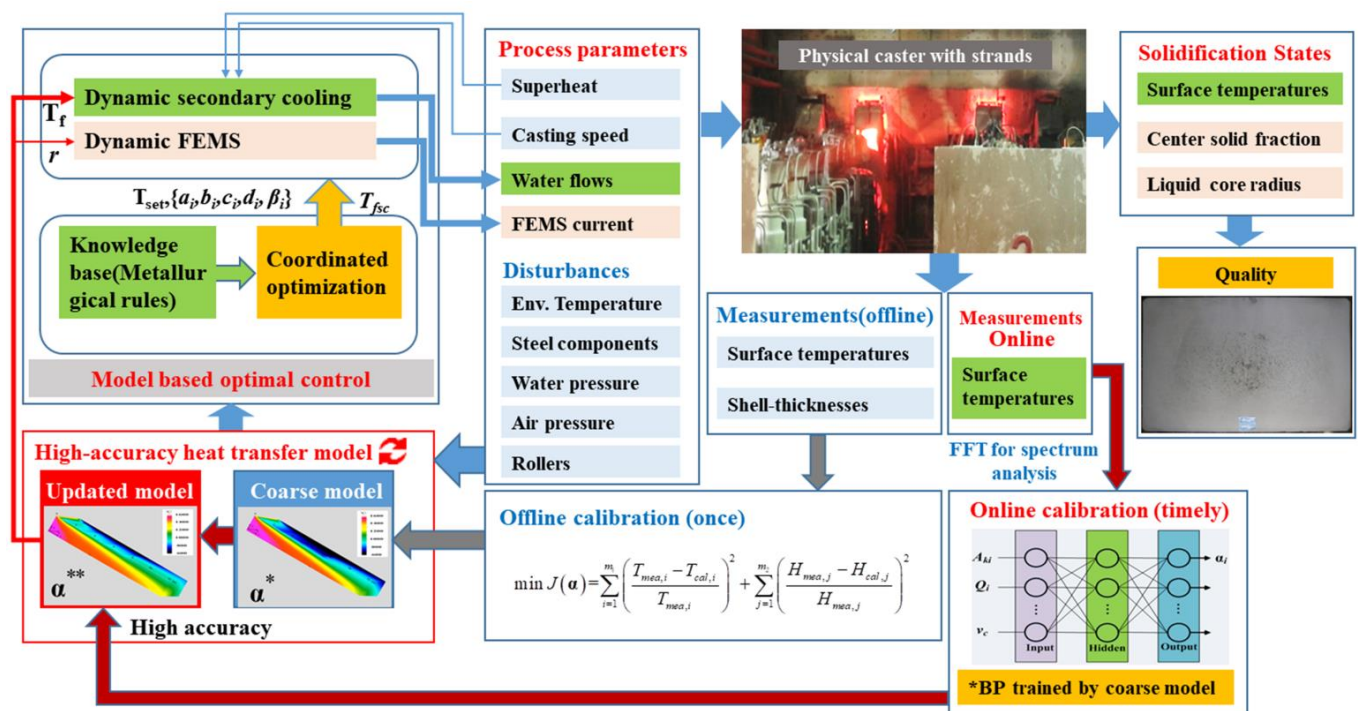


Figure 2. Intelligent optimal control strategy based on high-accuracy model.

At present, there is no unified definition of digital twins, in fact, but it is generally believed that digital twins should have four core elements: data, model, mapping, and interaction. In this framework, data include input measurements and process parameters; the model is a 3D real-time model, which maps the physical caster onto the digital world. Moreover, the optimal control and online measurement forms the interaction between physical world and digital world. Moreover, in the framework, there are four important factors selected as the key parameters, including superheat, casting speed, water flows, and FEMS current, for they are vitally related to the product quality. For secondary cooling, the water flows are most important; however, they are also related to the casting speed and superheat; for FEMS, there are three key factors influencing the metallurgical effect, including the stirring current, frequency and stirring mode (continuous or discontinuous (positive-stop-reverse)). Among them, the FEMS current is always adjustable.

3. Digital Twin for Heat Transfer Process

3.1. 3D Real-Time Model for All Stages

The heat transfer process for continuous casting of steel can be generally simplified as a “solid” heat transport problem under two assumptions: (1) increasing heat conduction induced by the flow of non-solid steel can be taken into account by an increased effective thermal conductivity; (2) the latent heat released during solidification can be considered

in equivalent specific heat. The governing equation then takes the following form in the follow-up coordinate system:

$$\rho c_{eff} \frac{\partial T}{\partial t} = \frac{\partial}{\partial x} \left(k_{eff} \frac{\partial T}{\partial x} \right) + \frac{\partial}{\partial y} \left(k_{eff} \frac{\partial T}{\partial y} \right) + \frac{\partial}{\partial z} \left(k_{eff} \frac{\partial T}{\partial z} \right) \quad (1)$$

where T is the temperature [$^{\circ}\text{C}$] and ρ is the density of the steel; $c_{eff} = dH/dT$, as c_{eff} is the equivalent specific heat, and H is the enthalpy; $k_{eff} = f_s k_s + m(1 - f_s)k_l$, as k_{eff} is the effective thermal conductivity, f_s is the solid fraction and k_s and k_l are, respectively, the thermal conductivity of the solid phase and liquid phase; and, significantly, m indicates the convection intensity of the non-solid part. Properties including ρ , H , f_s , k_s and k_l are assumed to be functions of T and of the steel compositions. For carbon and low-alloy steels, they can be calculated by our specially designed algorithm based on the pseudo-binary phase diagram [19]; others can be obtained by software JMatPro (Sente Software Ltd., Guildford, UK). In Equation (1), for simplification, the shrinkage is not considered.

In the model, the casting strand is divided into a queue of slices with height dz . Considering the symmetry, only one quarter of the cross section is selected to be the calculation domain. The initial condition of each slice is assumed to be the casting temperature:

$$T(x, y, z, 0) = T_c \quad (2)$$

For the steady casting stage, which takes up most of the casting time, boundary conditions are specified as follows:

- (1) In the mold [20]:

$$q = A - B\sqrt{t} \quad (3)$$

where q is boundary heat flux, t is the dwell time of the slice in the mold, and A and B are machine-dependent parameters.

- (2) In the secondary cooling zones (SCZ), water cooling and thermal radiation have been considered:

$$q = h_i(T - T_w) + \varepsilon\sigma \left[(T + 273)^4 - (T_a + 273)^4 \right] \quad (4)$$

where q is the boundary heat flux, h is the heat transfer coefficient, ε is the emissivity of the strand surface, σ is the Stefan–Boltzmann constant, T_w is the water temperature and T_a is the ambient air temperature. In SCZ, we set $\varepsilon = 0.85$.

There are two kinds of sprays in different secondary cooling zones: one is the water spray, and the other is the air-mist sprays, and the heat transfer coefficients for them are respectively expressed as Equations (5) [21] and (6) [22].

$$h_i = \frac{1570w_i^{0.55}(1 - 0.0075T_w)}{\alpha_i} \quad (5)$$

$$h_i = \frac{1000w_i}{\alpha_i} \quad (6)$$

where w_i is the water flow density ($\text{L}/\text{m}^2/\text{s}$) of cooling zone i , and α_i is the machine-dependent parameter for zone i .

- (3) In the air cooling zone (ACZ), thermal radiation has been considered:

$$q = \varepsilon_a\sigma \left[(T + 273)^4 - (T_a + 273)^4 \right] \quad (7)$$

where ε_a is the emissivity of the strand surface in ACZ.

For the initial casting stage and the final stage, there are additional conditions. Firstly, during the initial casting stage, for the dummy bar, the initial condition for extra slices of the dummy bar is $T(x, y, z, 0) = T_e$, where T_e is room temperature, and the flux of surfaces, except

its top surface and symmetric surfaces, are set to be radiative, with emissivity $\varepsilon_b = 0.7$. In the mold, $T(x,y,z,0) = T_c$. Furthermore, if we are considering the mold cooling during the fulfilling process at the very beginning of the initial stage, the transient short-time filling process can be treated as a moving process equivalent to that of the heat transfer. Secondly, during the final casting stage, when the tundish stops pouring the top surface of the strand then moves together with the entire strand, until it moves out of the calculation domain. The final casting stage lasts several minutes. In this stage, the boundary condition of the strand top surface changes to being radiative, with emissivity $\varepsilon_u = 0.7$.

Equations (1)–(7) plus additional conditions define the heat transfer model of continuous casting. The partial differential equation model can be discretized using the finite volume method (FVM) and solved using the alternative direction implicit (ADI) algorithm [22]. In the FVM-ADI algorithm, the heat transfer model is discretized to difference equations by the integration of the finite volume of each node in the slice from t to $t + \Delta t$, as Equation (8). For real-time, non-uniform grids and variable time steps are adopted and improved for greatly reducing the number of nodes in the 3D calculation domain [22,23]. Moreover, the heat transfer in the z direction can be treated as the source item. The newly developed heat transfer model is called Neucast-3D, while the former 2D one is called Neucast-2D.

$$\int_d^u \int_s^n \int_w^e \int_t^{t+\Delta t} \rho c_{eff} \frac{\partial T}{\partial t} dt dx dy dz = \int_t^{t+\Delta t} \int_d^u \int_s^n \int_w^e \left[\frac{\partial}{\partial x} \left(k_{eff} \frac{\partial T}{\partial x} \right) + \frac{\partial}{\partial y} \left(k_{eff} \frac{\partial T}{\partial y} \right) + \frac{\partial}{\partial z} \left(k_{eff} \frac{\partial T}{\partial z} \right) \right] dx dy dz dt \quad (8)$$

where w, e, s, n, d , and u are the interfaces of neighbor volumes and Δt is the time step.

3.2. Offline Calibration

In the numerical model described in Equations (1)–(8), there are some machine-dependent parameters appearing in the thermo-physical properties and boundary conditions, including m, A, B, α_i s and ε_n . For the model's high accuracy, they should be calibrated according to the field measurements before application.

Firstly, the parameters A and B appearing in the mold flux are determined by the energy conservation method:

$$\bar{q} = \frac{\rho_w Q_w c_w \Delta T_w}{F} = A - \frac{2}{3} B \sqrt{\frac{l_{meff}}{v_c}} \quad (9)$$

where l_{meff} is the effective mold length, $\rho_w, Q_w, c_w, \Delta T_w$ are respectively the density, flow, specific heat and in-out temperature difference of mold cooling water, and F is the heat exchange area.

The rest of the parameters are noted as vector α , where $\alpha = [\alpha_1, \alpha_2, \alpha_3, \alpha_4, \alpha_5, \varepsilon_n, m]$. With the surface temperature measurements using a two-color pyrometer (HWSG-2H) and shell thickness measurements using nail-shooting (type: ZG219), α can be calibrated by minimizing the following objective function:

$$J(\alpha) = \sum_{i=1}^{m_1} \left(\frac{T_{mea,i} - T_{cal,i}}{T_{mea,i}} \right)^2 + \sum_{j=1}^{m_2} \left(\frac{H_{mea,j} - H_{cal,j}}{H_{mea,j}} \right)^2 \quad (10)$$

where $T_{cal,i}$ and $T_{mea,i}$ are, respectively, calculated and measured temperatures, while $H_{cal,j}$ and $H_{mea,j}$ are calculated and measured shell thicknesses, respectively; m_1 is the count of the measuring positions for surface temperatures and m_2 is the count of the measuring positions for shell thicknesses. During the calibration process, shell thickness is not very conveniently measured, but it is very important for indicating the inner state of the bloom, which is especially vital for the calibration of the m value.

The above minimum optimization problem can be solved using the chaos particle swarm optimization algorithm (CPSO) [24]. The offline calibration contributes to the initial accuracy of the heat transfer model before online calibration.

3.3. Positive Online Calibration

Beyond offline calibration, online calibration is required for keeping the high accuracy of the digital twin model, since the machine-dependent parameters may change due to disturbances such as water temperature, water pressure, and so on. Therefore, a specially designed positive online calibration method [25] was developed, which is based on reliable online surface temperature measurements with a range of 800–1200 °C and stability within ±5 °C [26,27].

The online calibration method contains two related parts, as shown in Figure 3: the spectrum analysis conducted in the physical world and the prediction functions generated in the digital world.

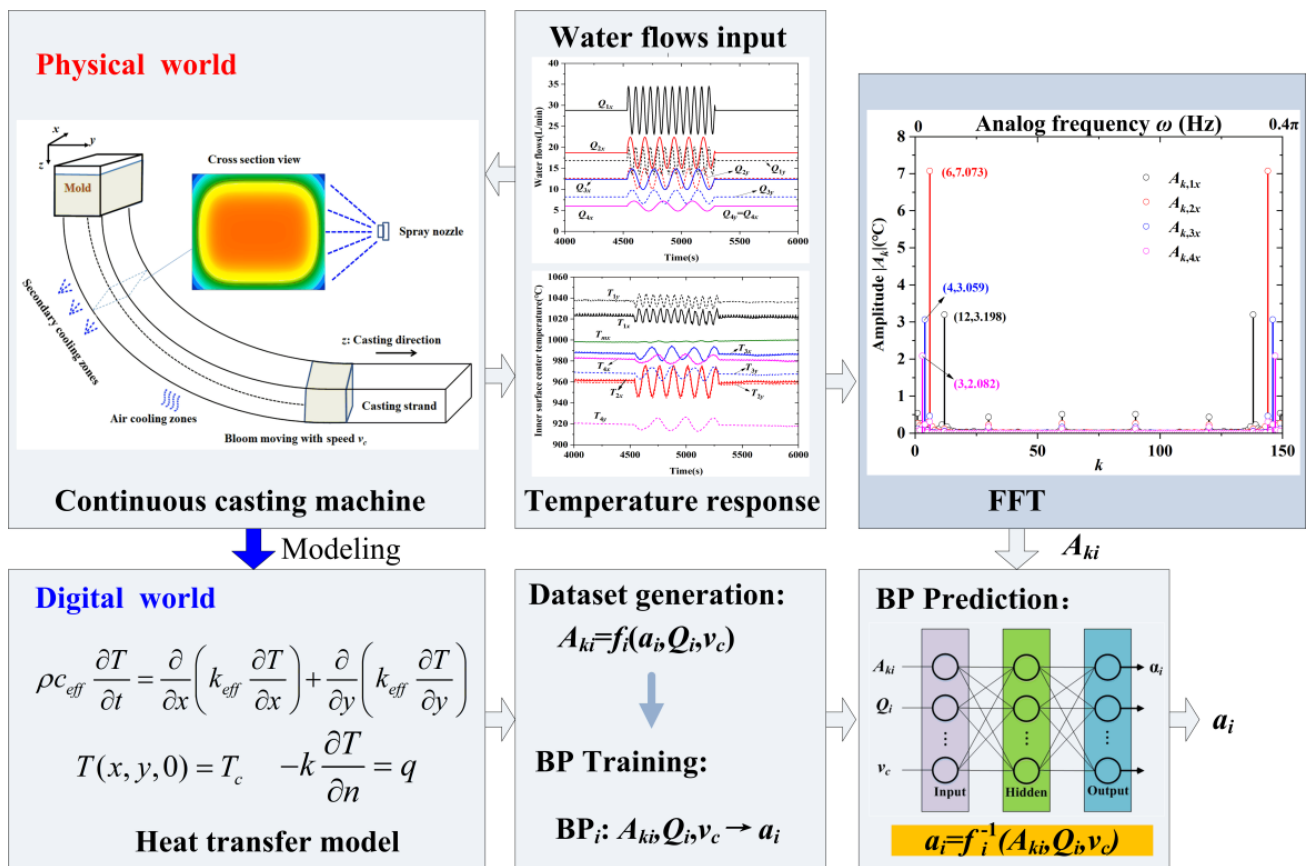


Figure 3. Online calibration method.

In the physical world, in order to obtain the transfer matrix from water flows to temperatures, extra water flows in sine-wave form are positively applied to excite the temperature responses for a limited period lasting for several minutes only each time (for example, 200 s for the billet caster or 1000 s for the bloom caster). The different cooling zones in the spectra are calculated separately, using fast Fourier transform (FFT) from the temperature responses, while the temperature responses are excited by extra water flows as inputs in sine-wave form. These extra water flows are designed with different frequencies for different cooling zones, so that their responses can be distinguished in the spectrum. For each cooling zone, the characteristic amplitude of each spectrum is related to machine-dependent parameters; more exactly, it is almost directly related to the corresponding a_i . During the spectrum analysis, there are two requirements for temperature measurements. Firstly, the amplitude of the interfered part of the noise spectrum's should be less than 0.2 °C to ensure the signal-to-noise-ratio (SNR, ≥ 10) requirement. Secondly, the maximum frequency of the main part of the noise spectrum is below the minimum frequency of input signals (for example, 1/16 Hz for the billet or 1/40 Hz for the bloom).

In the digital world, the prediction functions take characteristic amplitudes as inputs to calculate α_i s. In this paper, each of the prediction functions, mapping the characteristic amplitude A_{ki} to α_i , is established based on a BP network, while the BP network is trained by the dataset $\{<Q_i, v_c, A_{ki}, \alpha_i>\}$, where Q_i is the water flow of the secondary cooling zone i , and v_c is the casting speed. Each BP network is composed of three inputs, five hidden layers, one output layer, and one output, and the activation function is sigmoid. The BP network establishes a functional relationship between α_i and $<Q_i, v_c, A_{ki}>$. As for each $<Q_i, v_c, A_{ki}, \alpha_i>$, it is generated by model simulation with extra sine-wave inputs. In this way, α_i s can be updated online.

In the studied bloom caster, there are four sections in the SCZ. For each BP neural network, 1232 data sets were used for data training, where the discrete variables Q_i, v_c and α_i for interpolation were, respectively, eleven levels, seven levels and sixteen levels, as they were uniformly distributed in their own range.

3.4. Example Model Results

Figures 4 and 5 show the model results of a bloom caster. After calibration, surface temperature errors of the online model from measurements are within $\pm 10^\circ\text{C}$. In Figure 5, the casting starts from $t = 0$, the superheat is $35 \pm 10^\circ\text{C}$ and the casting speed is changed from 0.51 m/min to 0.54 m/min at $t = 2400$ s. Moreover, the cover effect is considered. The temperature increase is due to three reasons: (1) the strand head is in a lower temperature, due to the cold dummy bar; (2) increasing casting speed; (3) the cover effect, as the covers become warmer and warmer once the casting begins, and the radiation from the cover reduces the effective emissivity of the strand surface.

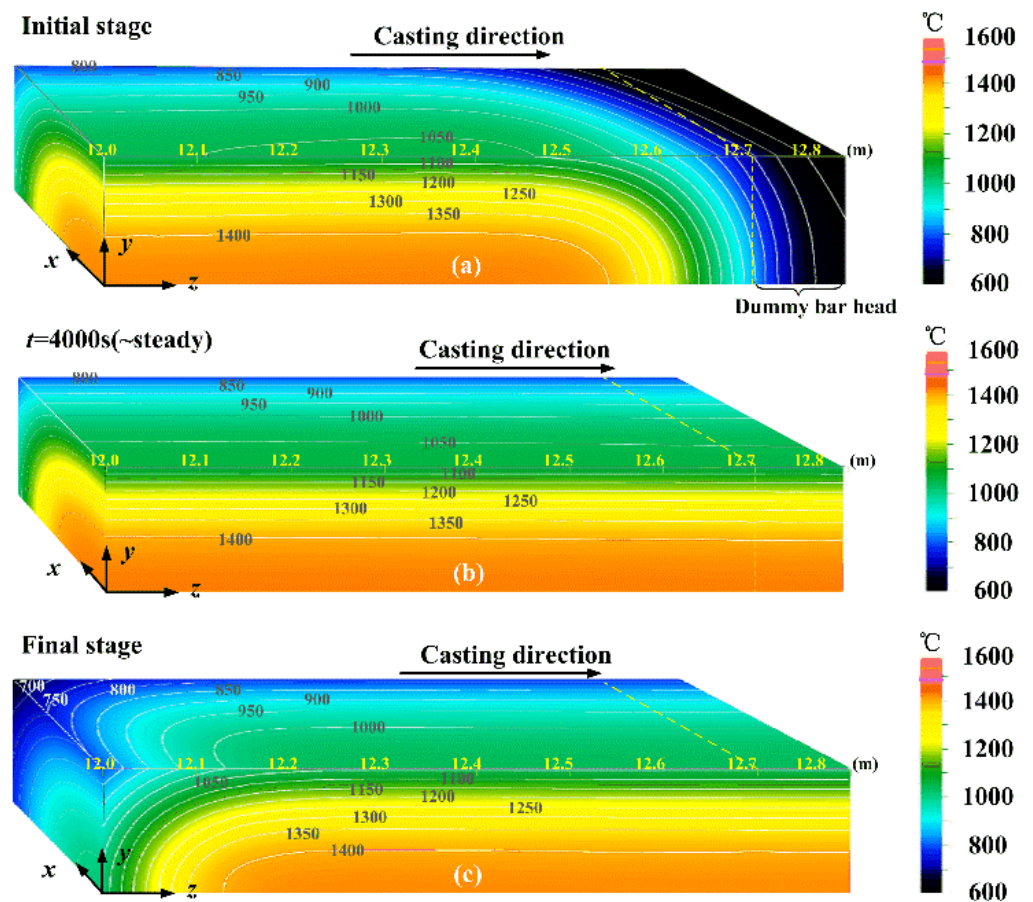


Figure 4. Calculated time-variant temperature field. (a) Initial stage; (b) after 4000 s; (c) final stage.

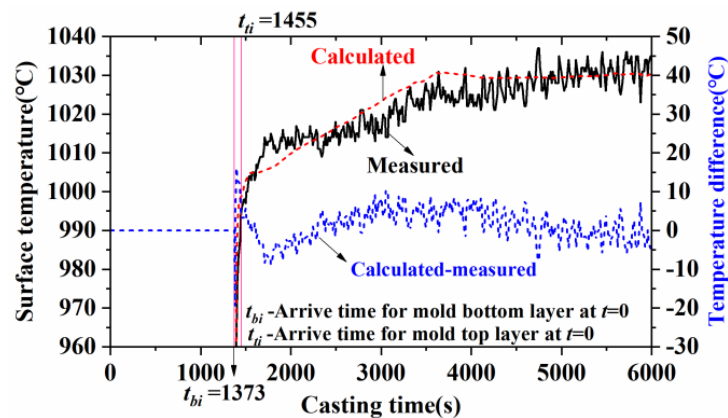


Figure 5. Calculated surface-center temperatures vs. measurements at $z = 12$ m (distance from meniscus).

4. Rule-Based Coordinated Optimization

4.1. Metallurgical Rules

At present, the mechanism of the continuous casting process is not yet entirely clear, and essentially the applied systems for the process are mostly knowledge-based, especially the metallurgical principles related to strand quality.

Firstly, cracks are one of the most common defects during continuous casting. The essential reason for a crack is that the stress (or strain) exceeds the strength of the steel. Figure 6 shows the high-temperature strength of different steels, including GCr15, 45# and 20# [28]. To avoid surface cracks, surface temperatures during the continuous casting process are supposed to avoid the temperature band with low ductility ($RA < 60\%$), about $700\text{--}900$ °C. The low ductility is mainly due to the decomposition of austenite (γ phase) and the newly generated α phase, as the strength of the α phase is only about one-quarter of the strength of the γ phase [29].

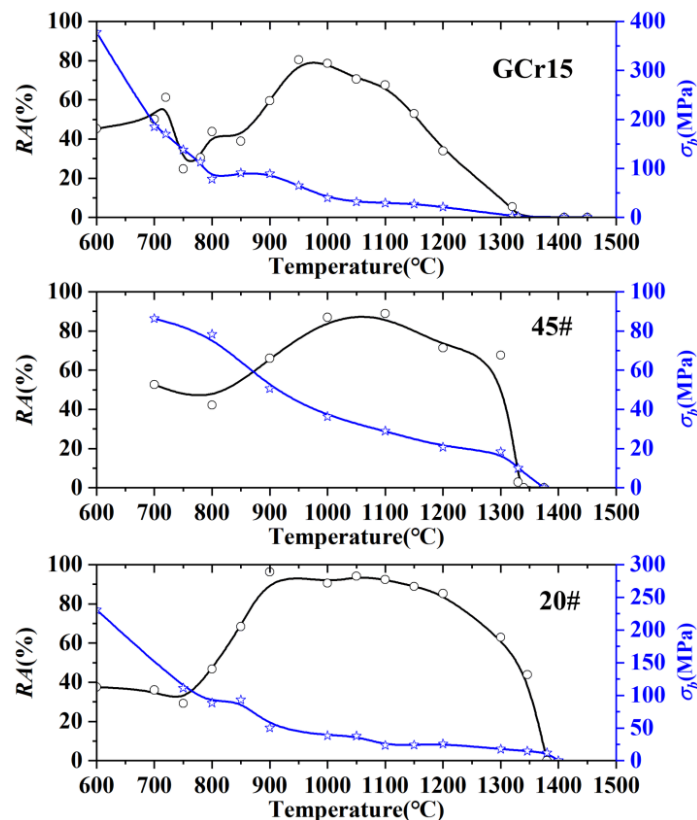


Figure 6. High-temperature strength of steels.

Secondly, center quality is greatly influenced by the FEMS. In the FEMS, a proper center temperature is required for good quality, as the temperature is related to solid fraction and viscosity. In fact, solid fraction is a monotonically decreasing function of temperature for certain steel. The relationships between viscosity and solid fraction for different steels are shown in Figure 7. For the FEMS, a too-low center temperature results in a too-high solid fraction and too-high viscosity; even the central part cannot be stirred any more, and neither can the other parts. Otherwise, the reverse happens, and a too-high center temperature is not good either, because the strand passes through the FEMS and there is still a large area of the central part not solidified, and this will reduce the positive metallurgical effect of the FEMS on improving the quality of the central part. Therefore, the recommended center solid fraction for the FEMS is between 0.3 and 0.4.

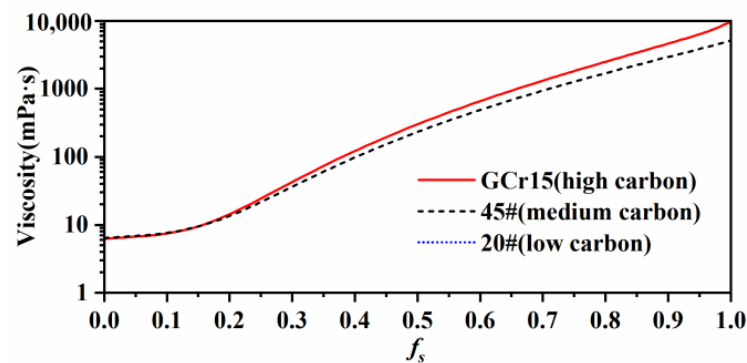


Figure 7. Viscosity variation with solid fraction.

4.2. Target Temperatures

According to the metallurgical rules related to cracks and central defects, some key temperatures obviously influence the strand quality, including the decomposition temperature of austenite, noted as A3, and the temperature for the solid fraction 0.35. These basic data can be calculated based on the pseudo-binary phase diagram [19] or JMatPro, as listed in Table 1. In addition, the components of typical steels are listed in Table 2.

Table 1. Key temperatures for different steels.

Temperature	GCr15 (°C)	45# (°C)	20# (°C)
A3	883 *	770	835
$T_{f_{sc}}^*(f_s = 0.35)$	1428	1471	1505

*—calculated using JMatPro software.

Table 2. Components of steels.

Element	GCr15 (%wt)	45# (%wt)	20# (%wt)
C	0.974	0.46	0.21
Si	0.226	0.26	0.29
Mn	0.316	0.680	0.50
P	0.011	0.035	0.011
S	0.002	0.025	0.006
Cr	1.454	0.046	-
Mo	0.005	-	-
Ni	0.045	0.04	0.04
Cu	0.063	0.16	-

%wt, weight percentage.

Moreover, the target surface temperatures also depend on the temperature at the exit of the mold, due to continuity.

$$T_{target,i} = T_{mold} + \frac{z_i - z_{mold}}{z_N - z_{mold}} (T_{target,N} - T_{mold}) \quad (11)$$

where $T_{target,i}$ is the target center surface temperature for the secondary cooling zone i , z_i is the end position of the secondary cooling zone i , T_{mold} is the center surface temperature at the exit of the mold, and N is the total number of secondary cooling zones. $T_{target,N} = A3 + \Delta T$, where ΔT is the temperature difference between corner and surface center, and $\Delta T = 150\sim 250$ °C.

4.3. Mathematical Description

4.3.1. Multi-Objective Functions

(1) Target surface temperatures

In each zone of the SCZ, cooling water is dispersed to the strand surface. Target temperatures are specified for the strand center surface at the end of each zone. Water flow-rate Q_i ($i = 1, 2, 3, \dots, N$) should be tuned in such a way that the resulting strand surface temperatures match the target temperatures as closely as possible. Formally, a cost function is introduced to evaluate the differences between the actual and target temperatures. It is defined as:

$$\min f_1 = \sum_{i=1}^N \lambda_i (T_i - T_{target,i})^2 \quad (12)$$

where N denotes the total number of zones, and T_i is the strand surface center temperature at the end of zone i .

(2) Target center temperature

Center temperature is related to viscosity and FEMS. In order to ensure flow ability for the final electromagnetic stirring, the target center temperature is defined as the middle position of the FEMS. The corresponding cost function f_2 is defined as Equation (13).

$$\min f_2 = (T_{fsc} - T_{fsc}^*)^2 \quad (13)$$

(3) Maximum casting speed

Besides the quality, maximum production is also pursued:

$$\max f_3 = v_c \quad (14)$$

4.3.2. Constraints

The technological constraints include the water flow Q_i , which has a lower and upper limit, depending on the hydraulic system. As to casting speed, for safe production, the thickness of the initial shell at the mold exit should be greater than a safe value H_{safe} for avoiding breakout. Moreover, the metallurgical length L_M has upper limits corresponding to the straightening point. In detail, the constraints can be written as Equation (15).

$$\begin{cases} Q_{imin} \leq Q_i \leq Q_{imax} \\ H_{mold} \geq H_{safe} \\ L_M < L_d \end{cases} \quad (15)$$

where Q_{imin} , Q_{imax} are the lower limit and the upper limit, respectively, of water flow for the i th secondary cooling zone.

For different steels, the relevant quality problem to be solved is also different. Therefore, the weight coefficients in the process of optimization should be changed accordingly.

4.3.3. Optimization Variables

The optimization variables are those flexible operating parameters strongly influencing the objective functions, including water flows, casting speed, superheat (or casting

temperature) and even the FEMS position if the FEMS is allowed to move along the caster and to be reinstalled. For different casters, the optimization variables are different.

4.4. Solving the Optimization Problem

4.4.1. Unified Objective Function

Different weights and the penalty function method are used separately for unifying the multiple objectives and constraints:

$$\min J = f_1 + \lambda_{fsc} f_2 - \lambda_v f_3 + \lambda_{st} \cdot \mathbf{f}_{st} \quad (16)$$

where f_i is defined in Section 4.3, for different objectives, and λ_i is the corresponding weights. Specifically, \mathbf{f}_{st} represents the objectives due to the constraints (Equation (15)).

Then the problem is simplified as a single objective problem, essentially without constraints.

4.4.2. Chaos Particle Swarm Optimization

Equation (16) defines the equivalent optimization problem. Since it is nonlinear and with multi-variables, CPSO [23] is adopted to solve the problem, in which the vectors of optimal variables are treated as the particles. Note $\mathbf{x} = (Q_1, Q_2, \dots, Q_N, v_c, \Delta T_c, z_{fems})$, when the FEMS is not movable, then $\mathbf{x} = (Q_1, Q_2, \dots, Q_N, v_c, \Delta T_c)$. The particles are refreshed by the following Equations (17) and (18):

$$v_{i,d} = wv_{i,d} + c_1 r_1 (p_{i,d} - x_{i,d}) + c_2 r_2 (g_d - x_{i,d}) \quad (17)$$

$$x_{i,d} = x_{i,d} + v_{i,d} \quad (18)$$

where i is the index of particle, d is the index of variables, w is the inertia weight, c_1 and c_2 are positive constants, r_1, r_2 are random numbers between 0 and 1, p_i is the best position of particle i and \mathbf{g} is the global best position of all particles.

To avoid falling into the local minimum, chaos mechanism is adopted when particles become stuck up to N_c times, as in Equation (19) (the Logistic iteration) and Equation (20) [24].

$$y_{k+1,d} = 4y_{k,d}(1 - y_{k,d}) \quad (19)$$

$$x_{i,d}^k = x_{i,d} + R_d(2y_{k,d} - 1) \quad (20)$$

where $y_{k,d}$ is between 0 and 1. The chaos mechanism based on Logistic iteration extends the exploration scope of the stuck particles.

In our study, $c_1 = 2.8$, $c_2 = 1.3$, $w = 0.5$, and $R_d = 1$. In addition, the particle number is $N_p = 100$, the maximum iterations $N_{max} = 30$, and the stuck count $N_c = 5$.

4.4.3. Example Optimization Result

An example optimization result for GCr15 is shown in Table 3 and Figure 8. Notice that there are slight differences between the T_{target} s and T_{set} s (the optimized setpoint values for surface temperatures). For the bloom caster, we chose a weak cooling mode: $\Delta T = 150$ °C. Table 4 shows the optimized water table for GCr15 under superheat = 25 °C.

Table 3. Target temperatures for GCr15.

Zone	T_{target}	T_{set}	Zone	T_{target}	T_{set}
1IO	996	996	1N	1006	1006
2IO	1003	1003	2N	1011	1011
3IO	1014	1014	3N	1019	1019
4IO	1024	1024	4N	1026	1026
5IO	1033	1030	5N	1033	994
FEMS center	1428	1429			

Unit: °C; IO–inner and outer sides; N–narrow sides; Optimized casting speed $v_c = 0.54$ m/min.

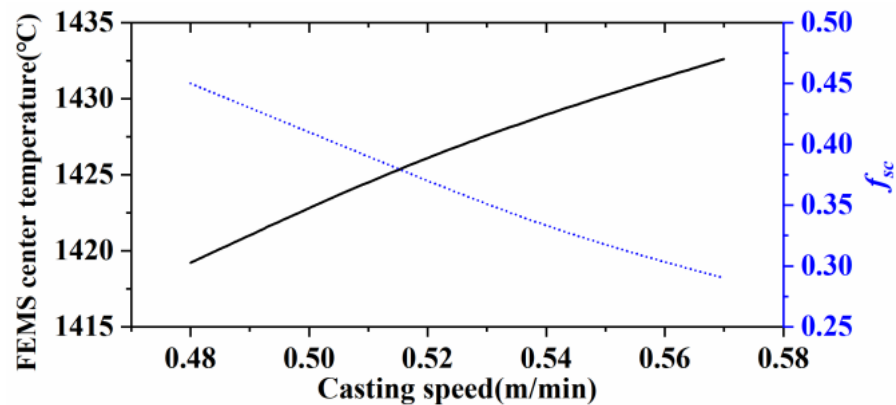


Figure 8. FEMS center temperature under different casting speeds.

Table 4. Optimized water table for GCr15.

Zone and Side	Casting Speed (m/min)			
	0.48	0.51	0.54	0.57
1IO	42.15	45.95	49.85	53.87
1N	26.37	28.82	31.38	34.07
2IO	14.35	15.25	16.15	17.04
2N	8.92	9.56	10.19	10.81
3IO	10.11	11.18	12.24	13.31
3N	4.37	5.29	6.16	7.00
4IO	2.39	3.16	3.88	4.55
4N	0	0	0.14	0.78
5IO	0	0	0	0
5N	0	0	0	0

Unit for water flows: L/min; superheat = 25 °C.

5. Dynamic Control of Secondary Cooling

5.1. Dynamic Feedforward Control

After optimization, water flows can be calculated using the immediate casting speed and immediate superheat. This is the static feedforward control mode. However, there are obvious disadvantages to the static mode: (1) A sudden change in casting speed can cause obvious temperature fluctuations. For example, when the casting speed changes increasingly and suddenly, water flows will increase immediately, accordingly. In the transient process, the response of the water flow is much faster than that of the casting speed, so there will be a valley appearing in the integral temperature response; otherwise, the reverse will happen. (2) There are obvious delays between immediate superheat and water flows.

In the dynamic feedforward control, instead of immediate casting speed and immediate superheat, effective casting speed and effective superheat are introduced to conquer the transient fluctuation in surface temperatures caused by the sudden change in casting speed and superheat. Both the effective casting speed and effective superheat are calculated using the slice model. There are three properties added which accompany each slice, since it is generated on the meniscus (the topmost surface of the strand), including position z_j , generated time t_j and initial superheat ΔT_{0j} . Therefore, effective casting speed and effective superheat can be calculated respectively by Equations (21) and (22).

$$v_{ei} = \sum_j z_j / \sum_j t_j \quad (21)$$

$$\Delta T_{ei} = \sum_j \Delta T_{0j} / ns_i \quad (22)$$

where ns_i is the slice number in the secondary cooling zone i .

5.2. Model-Based Feedback Control

Feedback control of secondary cooling is designed to keep surface temperatures extremely stable once there are control errors. The conventional control of secondary cooling does not contain the feedback control part, and when the disturbances happen the fluctuation will certainly be induced. In addition, it is bad for the quality of the stability.

In the feedback control, there are three important related aspects: setpoints, feedback signals and controllers. Among these, the setpoints are given by the former optimization process and the feedback signals are provided by the updated real-time heat transfer model. Instead of the hardware measurements, soft sensing of surface temperatures by the digital twin model provides a more effective way for obtaining feedback of surface temperatures, as it has some obvious advantages: low cost, no noise and robustness.

As for the controllers, we have developed a new design method in this paper, which is based on the transfer matrix from water flows to surface temperatures, noted as \mathbf{G} .

$$\Delta \mathbf{T} = [\Delta T_1, \Delta T_2, \dots, \Delta T_n]^T = \mathbf{G} \cdot \Delta \mathbf{Q} \quad (23)$$

$$\mathbf{G} = \begin{bmatrix} g_{11} & \dots & 0 & 0 \\ g_{21} & g_{22} & \dots & 0 \\ \dots & \dots & \dots & 0 \\ g_{n1} & g_{n2} & \dots & g_{nm} \end{bmatrix} \quad (24)$$

$$g_{ij} = \frac{\Delta T_i}{\Delta Q_j} = \frac{K_{ij}}{1 + t_{ij}s} e^{-\tau_{ij}s} \quad (i \leq j); \quad g_{ij} = 0 \quad (i > j) \quad (25)$$

where K_{ij} is the static gain expressed as $K_{ij} = g_{ij}(0)$, t_{ij} is the inertia time constant, s is the variable (complex number) for the Laplace transform, and τ_{ij} is the delay time. When $j = i$, $\tau_{ii} = 0$.

In the new method, the decoupling matrix is noted as \mathbf{H} and the diagonal matrix for the original transfer matrix is noted as \mathbf{D} , namely $\mathbf{D} = \text{diag}(\mathbf{G})$. Since $\mathbf{GH} = \mathbf{D}$, then $\mathbf{H} = \mathbf{G}^{-1}\mathbf{D}$. In the decoupling, since $\mathbf{G} \approx \mathbf{Gp}$, then $\mathbf{Gp} \cdot \mathbf{H} = \mathbf{Gp} \cdot \mathbf{G}^{-1}\mathbf{D} \approx \mathbf{GG}^{-1}\mathbf{D} = \mathbf{D}$, where \mathbf{Gp} is the matrix for the actual caster.

After decoupling, the cooling process turns into multiple single-input single-output (SISO) systems from the original multiple-input multiple-output (MIMO) system. As in Equation (24), each SISO subsystem for a certain cooling zone can be described by the first-order model without delay. Therefore, PI controllers for different zones can be specified as follows [30]:

$$K_{pi} = \frac{t_{ii}}{\gamma_i K_{ii}}, \quad T_{i,i} = t_{ii} \quad (26)$$

where γ_i is the speedup ratio for the closed-loop.

6. Dynamic Control of FEMS

6.1. Stirring Velocity of FEMS

The metallurgical effect of the FEMS is strongly related to the stirring intensity. Both the practice and theoretical analysis indicate that proper stirring intensity will obviously benefit the strand inner quality, such as in reducing the central positive segregation, while too-strong stirring may cause serious negative segregation in the solidification front, and too-weak stirring instead is useless.

The stirring intensity of the solidification front can be represented by the stirring velocity of molten steel. In the rotary stirring, the stirring flow velocity of the molten steel can be calculated by Equation (27) [1]:

$$v_{\max} = KB_m r \sqrt{f\sigma / \rho\mu^{0.44}} \quad (27)$$

where, K is the constant related to FEMS, B_m is the magnetic induction intensity of the cross-section center (Gs, 1 Gs = 0.1 mT = 0.0001 T), f is the frequency of the stirrer (Hz), r is the liquid core radius (mushy zone + liquid zone, cm), σ is the electric conductivity of the molten steel (s/cm), ρ is the molten steel density (g/cm³), and μ is the dynamic viscosity of the steel (CP, 1 CP = 0.001 Pa·s).

The relationship between the magnetic induction (B) at the stirrer center and the electric current (I) can be obtained from the measuring data, and B can be given as follows:

$$B_m = \varphi(f) I \quad (28)$$

Conventionally, the FEMS is static, since the electric current is static without changing during the casting process, no matter whether the casting speed changes or not. In the static mode, according to Equations (27) and (28), the stirring velocity will fluctuate when the casting speed or superheat changes, since the liquid core radius will change accordingly. The fluctuation is bad for the quality of the stability.

6.2. Magnetic Induction Measurement

In the caster, the magnetic induction intensity of the FEMS can be measured using a Tesla meter (also called a Gauss meter), such as the digital Tesla meter HT201. During the measurement, most importantly, the Hall probe should be well fixed. We designed a simple but effective method: firstly, a hard PVC pipe is used to fix the Hall probe; secondly, the pipe is fixed in the hole of a thick wooden board, of which the thickness may be up to several centimeters; finally, the wooden board is shaped as part of the circular truncated cone which can be put in the FEMS and kept steady. By pulling up or pushing down the PVC pipe, the magnetic induction intensity for different distances from the FEMS top can be measured. The method is shown in Figure 9. An example of the measured result is shown in Figure 10.

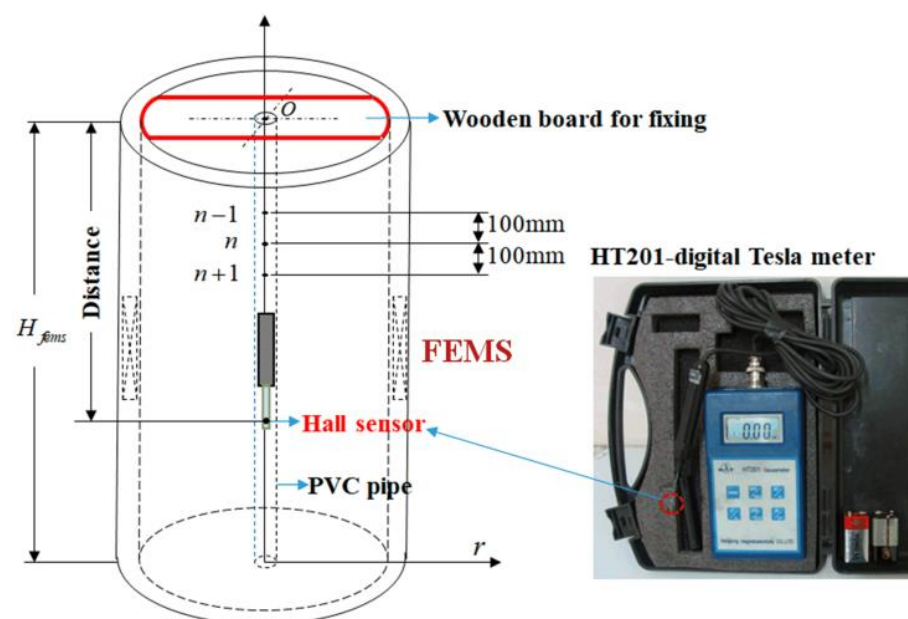


Figure 9. Measuring method and device for FEMS.

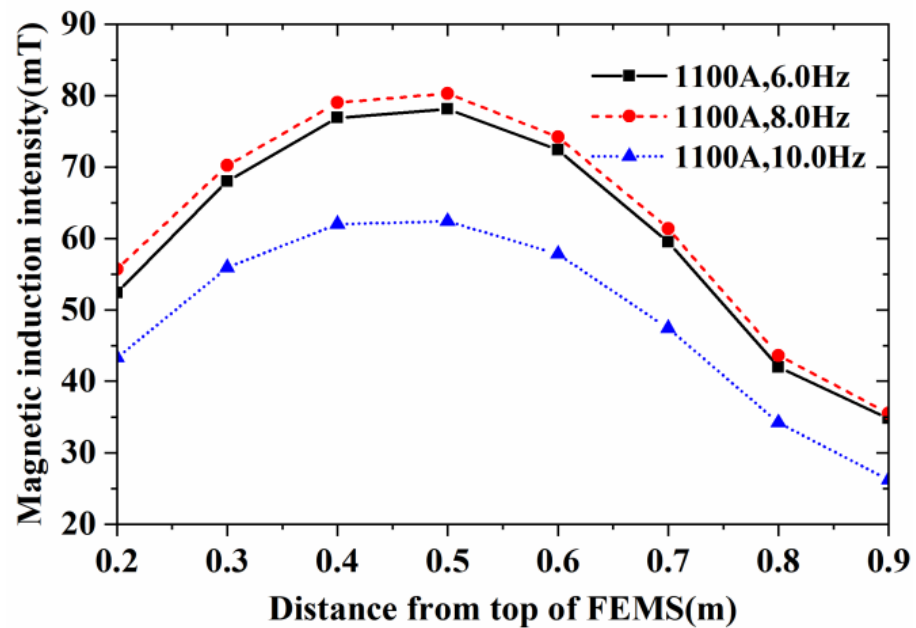


Figure 10. Measured magnetic induction intensity.

6.3. Dynamic Control of FEMS Current

The dynamic control of the FEMS is supposed to control the stability of the flow velocity during casting. In the practical application, a suitable operating frequency of the final electromagnetic stirrer has to be selected for maximum stirring velocity under the same electric current. For example, as shown in Figure 10, the best frequency is 8.0 Hz, since the value of B times the square root of frequency f is the greatest among the measured frequencies. In addition, the electric current value can be determined dynamically according to the corresponding liquid core radius and the target stirring velocity of the molten steel at the middle of the stirrer. The current can be calculated using Equation (29) [1], where the current I is inversely proportional to the liquid core radius r .

$$I = \frac{B_m}{\varphi(f)} = \frac{v_{\max}}{\varphi(f)K\sqrt{f\sigma/\rho\mu^{0.44}}} \frac{1}{r} \quad (29)$$

7. Results and Discussion

For industrial application, the presented optimal control strategy has been applied for improving the quality of steels in a bloom caster. In particular, GCr15 is taken as an example, and its components are listed in Table 1. Tables 5–7 show the other necessary conditions for calculation.

After optimization, since water flows corresponding to casting speed and superheat can be calculated by polynomial fitting, a new parametric water table can be obtained as seen in Table 8.

Table 5. Geometric parameters of studied caster.

Parameter	Value
Size (mm ²)	320 × 480
Radius (m)	12
Mold length (m)	0.8 (effective length: 0.7)
Lengths of SCZ (m)	[0.93,1.52,2.65,2.17,2.14]
FEMS position (m)	12.2 (fixed)

Table 6. Water table for GCr15 before optimization.

Zone and Side	Casting Speed (m/min)			
	0.48	0.51	0.54	0.57
1IO	28.8	28.8	28.8	28.8
1N	16.8	16.8	16.8	16.8
2IO	18.7	20.1	21.5	22.9
2N	12.6	13.6	14.6	15.6
3IO	12.4	13.4	14.4	15.4
3N	8.2	8.9	9.6	10.3
4IO	6	6	6	6
4N	6	6	6	6
5IO/5N	0	0	0	0

Unit for water flows: L/min; superheat = 25 °C.

Table 7. Calibrated parameters of model.

Parameters	Before Calibration	Calibrated Value
A (W/m ²)	2.68×10^6	1.546×10^6
B (W/(m ² ·s ^{1/2}))	3.35×10^5	1.067×10^5
α_1	4	3.788
α_2	1	1.043
α_3	1	1.043
α_4	1	1.043
α_5	1	1.043
ε_a	0.85	0.759
m	1	2.786

Table 8. Optimized coefficients for GCr15.

Zone	a_i	b_i	c_i	d_i	β_i	$T_{set,i}$
1IO	0	74.28	52.19	0.00	0.00698	996
1N	0	53.75	29.11	0.00	0.00724	1006
2IO	0	−0.01	29.90	0.00	0.00389	1003
2N	0	4.18	16.60	0.00	0.00366	1011
3IO	0	25.23	9.00	0.00	0.00507	1014
3N	0	34.91	−7.53	0.00	0.00524	1020
4IO	37.85	−7.19	−0.12	0.00	0.00853	1025
4N	46.14	−32.58	4.74	0.00	0.07582	1024
5IO	0	0	0	0	0	-
5N	0	0	0	0	0	-

$Q_i = (1 + \beta_i (\Delta T_{ei} - \Delta T_{std})) (a_i v^3 + b_i v^2 + c_i v + d_i)$ [L/min], where ΔT_{std} is the standard superheat depending on caster. For the studied bloom caster, $\Delta T_{std} = 30$ °C.

Figure 11 shows the surface center temperature of the inner side along the casting direction before and after optimization. After optimization, surface temperatures are very close to the targets, within ± 3 °C. Figure 12 shows the temperature field and solid fraction contour at the middle of the FEMS before and after optimization. After optimization, the main casting speed has been increased from 0.51 m/min to 0.54 m/min for the solid fraction which is closest to $f_{sc} = 0.35$.

Figures 13 and 14 show the dynamic control of the secondary cooling and FEMS current, respectively. In the dynamic control of the secondary cooling, surface temperatures are controlled precisely within ± 4 °C from the optimized setpoints. In the dynamic control of FEMS, the FEMS current varies with the liquid core radius, accordingly.

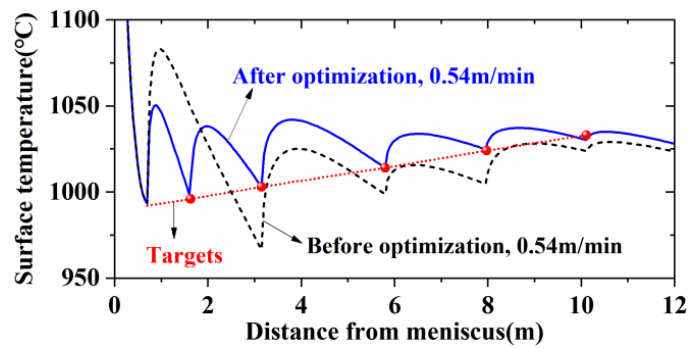


Figure 11. Temperatures before and after optimization.

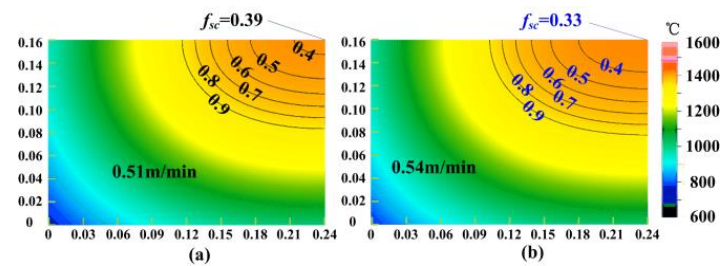


Figure 12. Solid fraction at the middle of FEMS: (a) before optimization; (b) after optimization.

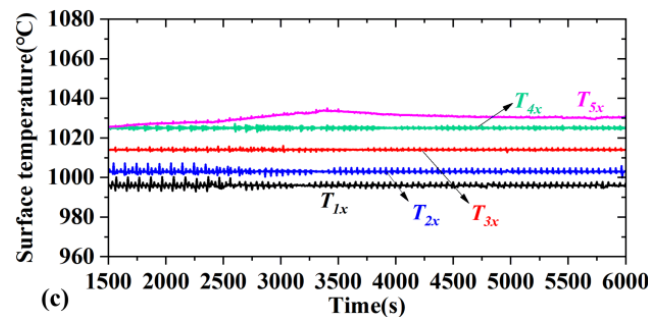
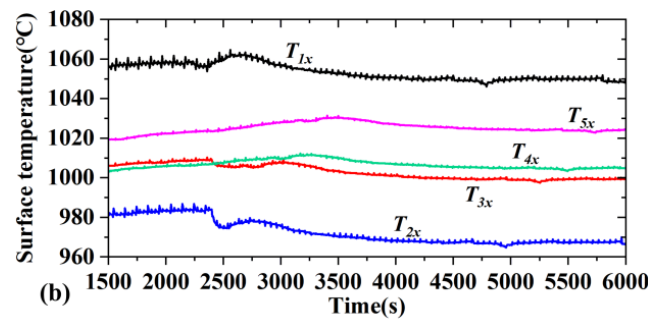
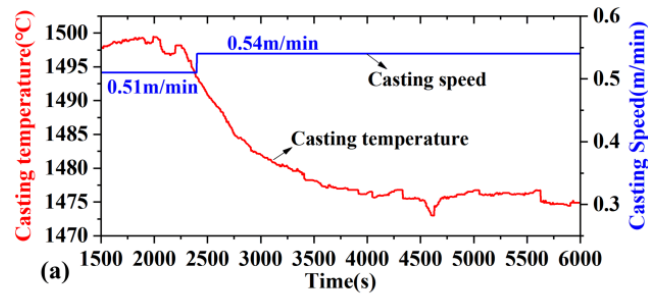


Figure 13. Surface center temperatures at the end of different zones: (a) casting conditions; (b) surface temperatures before optimization; (c) surface temperatures after optimization.

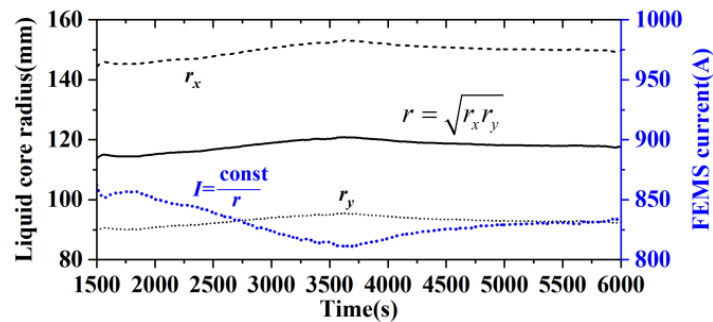


Figure 14. Dynamic control of FEMS current.

After optimal control, the central quality of the macrographs has obviously improved, typically as shown in Figure 15. From the statistics, after optimal control, the macro-segregation grades for the macrograph over 1.5 have been reduced from 11% (23 of 211 samples) to 3.3% (20 of 611 samples).

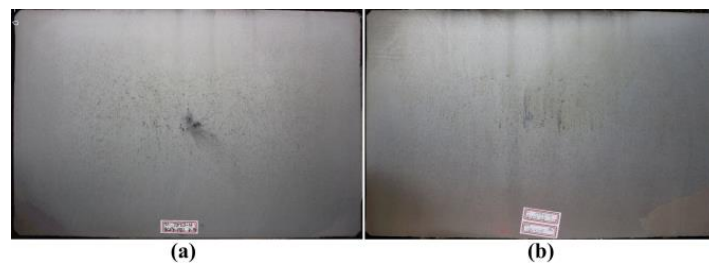


Figure 15. Macrographs: (a) before optimal control; (b) after optimal control.

8. Conclusions

- (1) A high-accuracy three dimensional real-time heat transfer model has been established as the digital twin of continuous casting; after offline calibration and online calibration, the calculated errors from measurements are within ± 10 °C.
- (2) Based on the digital twin model, an optimal control strategy has been presented, including coordinated optimization and dynamic control of secondary cooling and final electromagnetic stirring. Through optimal control, the targets and coefficients for control can be effectively optimized, and the temperatures can be well controlled within ± 4 °C.
- (3) Application indicates that the above methods are effective in improving the strand quality.

Author Contributions: Conceptualization, J.Y. and Z.J.; methodology, J.Y.; validation, J.Y. and W.L.; writing—original draft preparation, J.Y. and Z.J.; writing—review and editing, J.Y.; project administration, Z.X.; funding acquisition, J.Y. All authors have read and agreed to the published version of the manuscript.

Funding: This research was funded by the National Natural Science Foundation of China, grant number U21A20117, 52074081, 52074085, and 61703084. The APC was funded by U21A20117.

Data Availability Statement: The data presented in this study are available on request from the corresponding author. The data are not publicly available due to privacy.

Acknowledgments: The authors gratefully thank the financial support of the National Natural Science Foundation of China Grants U21A20117, 52074081, 52074085, and 61703084, and the research support of Nanjing Iron & Steel Cooperation (NISCO).

Conflicts of Interest: The authors declare no conflict of interest. The funders had no role in the design of the study; in the collection, analyses, or interpretation of data; in the writing of the manuscript, or in the decision to publish the results.

Nomenclature

T	Temperature	\mathbf{G}	Transfer function matrix
ρ	Density	g_{ij}	Transfer function
H	Enthalpy	K_{ij}	Static gain for transfer function
f_s	Solid fraction	t_{ij}	inertia time constant
k	Thermal conductivity	v_c	Casting speed
c_{eff}	Equivalent specific heat	ΔT_w	Mold in-out temperature difference
x,y,z	Coordinates	A_{ki}	Spectra amplitude
T_c	Casting temperature	v_{ei}	Effective casting speed
A,B	Mold cooling parameters	ΔT_{ei}	Effective superheat
α_i	Cooling parameter for Zone i	ΔT_{std}	Standard superheat
m	Convection-related parameter	B_m	Magnetic induction intensity
ε	Emissivity	c_w	Water specific heat
Q	Water flow	l_{meff}	Effective mold length
q	Boundary heat flux		
h	Heat transfer coefficient	Subscripts	
$H_{mea,j}$	Measured shell thickness	i	Zone number in SCZ
$H_{cal,j}$	Calculated shell thickness	a	Air cooling zone
$T_{mea,i}$	Measured surface temperature	w	water
$T_{cal,i}$	Calculated surface temperature	ij	Zone j affects Zone i
Q_w	Water flow in mold	$i = 1,2,3, \dots, N$	Specific zone number

References

- Mao, B.; Zhang, G.; Li, A. *Theory and Technology of Electromagnetic Stirring for Continuous Casting*; Metallurgical Industry Press: Beijing, China, 2012.
- Ji, C.; Deng, S.; Guan, R.; Zhu, M. Real-time heat transfer model based on distributed thermophysical property calculation for the continuous casting process. *Steel Res. Int.* **2019**, *90*, 1800476. [[CrossRef](#)]
- Yunwei, H.; Mujun, L.; Dengfu, C.; Kai, T.; Huamei, D.; Pei, X. Effect of hot water vapor on strand surface temperature measurement in steel continuous casting. *Int. J. Therm. Sci.* **2019**, *138*, 467–479.
- Ma, J.; Xie, Z.; Jia, G. Applying of Real-time Heat Transfer and Solidification Model on the Dynamic Control System of Billet Continuous Casting. *ISIJ Int.* **2008**, *48*, 1722–1727. [[CrossRef](#)]
- Louhenkilpi, S.; Mäkinen, M.; Vapalahti, S.; Räisänen, T.; Laine, J. 3D steady state and transient simulation tools for heat transfer and solidification in continuous casting. *Mater. Sci. Eng. A* **2005**, *413*, 135–138. [[CrossRef](#)]
- Blazek, K.; Moravec, R.; Zheng, K.; Lowry, M.; Gregurich, N.; Flick, G. New pseudo-3D dynamic secondary cooling model implementation and results at arcelormittal burns harbor. *Iron Steel Technol.* **2016**, *13*, 78–85.
- Thomas, B.G. Review on Modeling and Simulation of Continuous Casting. *Steel Res. Int.* **2017**, *89*, 1700312. [[CrossRef](#)]
- Zhao, Y.; Chen, D.F.; Long, M.J.; Shen, J.L.; Qin, R.S. Two-dimensional heat transfer model for secondary cooling of continuously cast beam blanks. *Ironmak. Steelmak.* **2013**, *41*, 377–386. [[CrossRef](#)]
- Hardin, R.; Du, P.; Beckermann, C. Three-dimensional Simulation of Heat Transfer and Stresses in a Steel Slab Caster. In Proceedings of the 4th International Conference on Modeling and Simulation of Metallurgical Processes in Steelmaking, Paper No. STSI-71, Steel Institute VDEh, Düsseldorf, Germany, 27 June–1 July 2011; pp. 1–6.
- Mauder, T.; Stetina, J. Optimization of the secondary cooling in a continuous casting process with different slab cross-sections. *Mater. Tehnol.* **2014**, *48*, 521–524.
- Zhai, Y.Y.; Li, Y.; Ao, Z.G. Optimization of continuous casting secondary cooling based on an enhanced multi-objective genetic algorithm. *J. Northeast. Univ.* **2019**, *40*, 658–662.
- Ma, J.C.; Lu, C.S.; Yan, Y.T.; Chen, L.Y. Design and application of dynamic secondary cooling control based on real time heat transfer model for continuous casting. *Int. J. Cast Met. Res.* **2013**, *27*, 135–140. [[CrossRef](#)]
- Petrus, B.; Zheng, K.; Zhou, X.; Thomas, B.G.; Bentsman, J. Real-time, model-based spray-cooling control system for steel continuous casting. *Metall. Mater. Trans. B Vol.* **2011**, *42*, 87–103. [[CrossRef](#)]
- Xiao, C.; Zhang, J.-M.; Luo, Y.-Z.; Wei, X.-D.; Wu, L.; Wang, S.-X. Control of Macrosegregation Behavior by Applying Final Electromagnetic Stirring for Continuously Cast High Carbon Steel Billet. *J. Iron Steel Res. Int.* **2013**, *20*, 13–20. [[CrossRef](#)]
- Su, W.; Wang, W.-L.; Luo, S.; Jiang, D.-B.; Zhu, M.-Y. Heat Transfer and Central Segregation of Continuously Cast High Carbon Steel Billet. *J. Iron Steel Res. Int.* **2014**, *21*, 565–574. [[CrossRef](#)]
- Luo, S.; Piao, F.Y.; Jiang, D.D.; Wang, W.L.; Zhu, M.Y. Numerical Simulation and Experimental Study of F-EMS for Continuously Cast Billet of High Carbon Steel. *J. Iron Steel Res. Int.* **2014**, *21*, 51–55. [[CrossRef](#)]
- Yu, Y.; Luo, X.; Zhang, H.; Zhang, Q. Dynamic optimization method of secondary cooling water quantity in continuous casting based on three-dimensional transient nonlinear convective heat transfer equation. *Appl. Therm. Eng.* **2019**, *160*, 113988. [[CrossRef](#)]

18. Wu, D.S.; Ji, Z.P.; Yang, J.; Gao, H.W.; Yu, J.H.; Ju, Z.J. Coordinated optimal control of secondary cooling and final elec-tromagnetic stirring for continuous casting billets. *J. Control Sci. Eng.* **2020**, *2020*, 1–9. [CrossRef]
19. Xie, Z.; Yang, J. Calculation of Solidification-Related Thermophysical Properties of Steels Based on Fe-C Pseudobinary Phase Diagram. *Steel Res. Int.* **2014**, *86*, 766–774. [CrossRef]
20. Savage, J.; Pritchard, W. The problem of rupture of the billet in the continuous casting of steel. *J. Iron Steel Inst.* **1954**, *178*, 269–277.
21. Nozaki, T.; Matsuno, J.-I.; Murata, K.; Ooi, H.; Kodama, M. A Secondary Cooling Pattern for Preventing Surface Cracks of Continuous Casting Slab. *Trans. Iron Steel Inst. Jpn.* **1978**, *18*, 330–338. [CrossRef]
22. Yang, J.; Xie, Z.; Ji, Z.; Meng, H. Real-time Heat Transfer Model Based on Variable Non-uniform Grid for Dynamic Control of Continuous Casting Billets. *ISIJ Int.* **2014**, *54*, 328–335. [CrossRef]
23. Yang, J.; Xie, Z.; Meng, H.J.; Liu, W.H.; Ji, Z.P. Multiple time steps optimization for real-time heat transfer model of continuous casting billets. *Int. J. Heat Mass Tran.* **2014**, *76*, 492–498. [CrossRef]
24. Meng, J.Y.H.J.; Ji, Z.P.; Xie, Z. Parameter identification of heat transfer model for continuous casting billets based on chaos particle swarm optimization. *J. Northeast. Univ. (Nat. Sci.)* **2014**, *35*, 613–616. (In Chinese)
25. Yang, J.; Xie, Z.; Hu, Z.W.; Wang, J.J.; Wei, W. Positive Online Calibration of Heat Transfer Model for Continuous Casting of Steel Based on Surface Temperature Measurement. 2022. Available online: <https://ssrn.com/abstract=4272505> (accessed on 9 November 2022).
26. Peng, W.; Zhi, X.; Zhenwei, H. Study on the multi-wavelength emissivity of GCr15 steel and its application on temperature measurement for continuous casting billets. *Int. J. Thermophys.* **2016**, *37*, 129.
27. Peng, W.; Zhenwei, H.; Zhi, X.; Ming, Y. A new experimental apparatus for emissivity measurements of steel and the application of multi-wavelength thermometry to continuous casting billets. *Rev. Sci. Instrum.* **2018**, *89*, 054903.
28. Gan, Y. *Practical Manual of Modern Continuous Casting of Steel*; Metallurgical Industry Press: Beijing, China, 2010.
29. Cai, K. *Quality Control of Continuous Casting Slabs*; Metallurgy Industry Press: Beijing, China, 2010.
30. Wang, F.-S.; Juang, W.-S.; Chan, C.-T. Optimal tuning of pid controllers for single and cascade control loops. *Chem. Eng. Commun.* **1995**, *132*, 15–34. [CrossRef]

Disclaimer/Publisher’s Note: The statements, opinions and data contained in all publications are solely those of the individual author(s) and contributor(s) and not of MDPI and/or the editor(s). MDPI and/or the editor(s) disclaim responsibility for any injury to people or property resulting from any ideas, methods, instructions or products referred to in the content.